5-21-2013

Micro Modeling Study of Cathode/Electrolyte Interfacial Stresses for Solid Oxide Fuel Cells

Xinfang Jin
University of South Carolina - Columbia, xfjin@sc.edu

Xingjian Xue
University of South Carolina - Columbia, xue@cec.sc.edu

Publication Info

Published in *Journal of The Electrochemical Society*, Volume 160, Issue 8, 2013, pages F815-F823.

Publisher's Version: http://dx.doi.org/10.1149/2.074308jes
Jin, X. & Xue, X. (21 May 2013). Micro Modeling Study of Cathode/Electrolyte Interfacial Stresses for Solid Oxide Fuel Cells. Journal of The Electrochemical Society, 160 (8), F815 – F823. http://dx.doi.org/10.1149/2.074308jes

Journal of The Electrochemical Society, **160** (8) F815-F823 (2013)
0013-4651/2013/160(8)/F815/9/$31.00 © The Electrochemical Society

Micro Modeling Study of Cathode/Electrolyte Interfacial Stresses for Solid Oxide Fuel Cells

Xinfang Jin and Xingjian Xue*,z

Department of Mechanical Engineering, University of South Carolina, Columbia, South Carolina 29208, USA

Delamination of the cathode/electrolyte interface is an important degradation phenomenon in solid oxide fuel cells (SOFCs). While the thermal stress has been widely recognized as one of the major reasons for such delamination failures, the role of chemical stress does not receive too much attention. In this paper, a micro-model is developed to study the cathode/electrolyte interfacial stresses, coupling oxygen ion transport process with structural mechanics. Results indicate that the distributions of chemical stress are very complicated at the cathode/electrolyte interface and show different patterns from those of thermal stress. The maximum principal stresses take place at the cathode/electrolyte interface and are affected by the distribution of oxygen vacancy concentration on the cathode particle surface. The model is able to readily study complicated interfacial stresses in SOFCs, which otherwise would be difficult for experimental techniques.
 [DOI: 10.1149/2.074308jes]

Manuscript submitted February 21, 2013; revised manuscript received May 10, 2013. Published May 21, 2013. This was Paper 2153 presented at the Honolulu, Hawaii, Meeting of the Society, October 7–12, 2012.

The basic structure of solid oxide fuel cells (SOFCs) is a positive electrode-electrolyte-negative electrode (PEN) tri-layer assembly, in which the dense electrolyte is sandwiched by porous electrodes on either side. Long-term stability is an important requirement for commercial applications of SOFC technology. However, very aggressive operating temperatures (600–1000°C) generally lead to a variety of SOFC degradations representing significant challenges in meeting lifetime requirements.[1] It is therefore essential to increase the understanding of the degradation mechanisms.

One of the important degradation phenomena in SOFCs is the occurrence of delamination at the oxygen electrode/electrolyte interface. Experimental observations have shown that such delamination failures occur in both fuel cell mode[2] and electrolysis mode.[3] Upon the occurrence of delamination, the cell performance degradation is accelerated because the interfacial open-gap, perpendicular to the main current path, consists of an insulating barrier to charge conduction, and destroys electrochemical reaction sites.[4] Such a mechanical degradation has been identified as a major limitation to the industrial developments of SOFCs.[5]

Thermal stresses have been widely recognized as one of the main factors leading to the structural failure of SOFCs.[6,7] Thermal stresses could be induced in the materials through several ways. During the cooling of the cell after being sintered at very high temperatures, stresses arise in the materials due to the mismatch in thermal expansion coefficients (TEC) between different layers of the cell.[7] Such stresses generated during cell fabrication processes are generally regarded as residual stresses. Residual stresses can also be expected if the cooling rates are not slow enough to sustain a quasi-steady heat transfer resulting in spatial temperature gradients.[8] The most widely investigated situations are thermal stresses induced by spatial temperature gradients during the fuel cell operations,[6–10] particularly in transient operating conditions.[11] If the fuel supply is accidentally stopped, the nickel cermet re-oxidation may occur. This re-oxidation step generates an anodic bulk expansion which can also lead to a high level of stresses in the cell layers.[12]

The mechanism governing the delamination at the oxygen electrode/electrolyte interface remains an active subject of debate. It is generally recognized that, for the stationary applications, the chemical instability at the interfaces is one of the key issues, whereas the thermo-mechanical instability is important in the transportation applications because of frequent thermal cycles.[10,13] Other understanding envisioned that the high pressure of oxygen generated at the interface could cause the delamination as well.[14]

SOFCs require materials with the ability to release or store oxygen in addition to a high concentration of oxygen vacancies for high oxygen ionic conductivity.[13] The transport of oxygen ion through oxygen vacancies may lead to the effect that the distribution of oxygen vacancy concentration is not uniform within the bulk materials, which would cause different volumetric expansions within the materials. As a result, chemical stress occurs in oxygen ionic conducting materials. In open literature, the thermal stress effects on SOFC structures have been investigated extensively, however, the chemical stress effects are rarely studied, particularly their effects on the delamination at the cathode/electrolyte interface. When the thermal stress is coupled with the chemical stress, the structural reliability issue of SOFCs will become even more complicated. The objective of this paper is to develop a micro model to study the complicated stress states at the cathode/electrolyte interface in SOFCs, including thermal stress and chemical stress. The results could be used to study the different roles of thermal stress and chemical stress at the cathode/electrolyte interface in SOFCs.

Modeling of Transport Process in Combination with Structural Mechanics

Solid mechanics.— The total strain is the summation of the mechanical strain and two types of eigenstrains,

$$\varepsilon_{ij} = \varepsilon_{ij}^{me} + \varepsilon_{ij}^{T} + \varepsilon_{ij}^{c} \quad [1]$$

Here ε is the strain, the superscripts *me*, *T*, and *c* represent mechanical, thermal, and chemical respectively.

For an isotropic material, the constitutive relationship for the strain ε_{ij}^{me} and the corresponding mechanical stress is given as:

$$\varepsilon_{ij}^{me} = \frac{1}{E}[(1+\nu)\sigma_{ij} - \nu\sigma_{kk}\delta_{ij}] \quad [2]$$

Where σ_{ij} represents the stress components with *i* and *j* indicating the axis of the Cartesian coordinate system, *E* is Young's Modulus, ν is Poisson's ratio of the material, and $\delta_{ij} = \begin{cases} 1, i = j \\ 0, i \neq j \end{cases}$, $\sigma_{kk} = \sigma_1 + \sigma_2 + \sigma_3$. In this paper, *E* and ν are treated as constants. The variations of the elastic constants with temperature and oxygen vacancy concentration are neglected.[15]

The eigenstrain ε_{ij}^{T} induced by temperature variations in an isotropic material is given by:

$$\varepsilon_{ij}^{T} = \alpha\Delta T\delta_{ij} \quad [3]$$

Where ΔT is the temperature variation, and α is the thermal expansion coefficient. It is worth noting that dopants may change the formation energy of defects in materials, which in turn can affect the dependence of defect concentration on temperatures and hence the practical thermal expansion coefficient. For simplicity, the true thermal

*Electrochemical Society Active Member.
zE-mail: Xue@cec.sc.edu

expansion coefficient is employed in this study, which is defined under the constant defect concentration of materials.[16]

The chemical expansion stress induced by oxygen vacancy variations is calculated by analogy to the thermal stress. It is assumed that the volume of ionic conducting bulk materials changes linearly with volumetric oxygen ion insertion and extraction. The eigenstrain ε_{ij}^{c} induced by chemical expansion effect is written as:[17]

$$\varepsilon_{ij}^{c} = \beta \Delta c \delta_{ij} \quad [4]$$

Where Δc is the variation of oxygen vacancy concentration, β is the chemical expansion coefficient.

Substitution of equations 2–4 into equation 1 leads to:

$$\varepsilon_{ij} = \frac{1}{E}[(1+\nu)\sigma_{ij} - \nu\sigma_{kk}\delta_{ij}] + \alpha\Delta T\delta_{ij} + \beta\Delta c\delta_{ij} \quad [5]$$

The expression for stress components can be written as,

$$\sigma_{ij} = 2\mu^{*}\varepsilon_{ij} + (\lambda\varepsilon_{kk} - \alpha'\Delta T - \beta'\Delta c)\delta_{ij} \quad [6]$$

Where $\mu^{*} = E/2(1+\nu)$, $\lambda = 2\nu\mu^{*}/(1-2\nu)$, $\alpha' = \alpha(3\lambda + 2\mu^{*})$, $\beta' = \beta(3\lambda + 2\mu^{*})$, and $\varepsilon_{kk} = \varepsilon_1 + \varepsilon_2 + \varepsilon_3$.

In elasticity, the strain tensor is related to the displacement **u** by:[18]

$$\varepsilon_{ij} = \frac{1}{2}\left(\frac{\partial u_i}{\partial x_j} + \frac{\partial u_j}{\partial x_i}\right) \quad [7]$$

By neglecting the body forces, the equilibrium equation is represented as,

$$\sigma_{ij,i} = 0\,(i, j = 1, 2, 3) \quad [8]$$

Substituting equations 6, 7 into equation 8, the displacement equation can be expressed as,[19]

$$\mu^{*}\nabla^{2}u_{\mathrm{i}} + (\lambda + \mu^{*})u_{\mathrm{k,ki}} - \alpha'\Delta T - \beta'\Delta c = 0, (i, k = 1, 2, 3) \quad [9]$$

Transport process in ionic conducting ceramic materials.— The electrochemical potential in an ideal solid solution can be expressed as,[17,20,21]

$$\mu_j = \mu_{0,j} + RT\ln x_j + z_j F\phi + \tau_j \quad [10]$$

Where μ_j is the electrochemical potential of species j; R the gas constant; T the temperature; x_j the molar fraction of species j; z_j the effective charge of species j; F the Faraday's constant; ϕ the potential; and τ_{j} is the stress-dependent part of the electrochemical potential. For isotropic elastic solids, the τ_{j} is given by,[17]

$$\tau_j = -\beta_j\left(\sigma_{kk} + \frac{3\nu}{2E}(\sigma_{kk})^2 - \frac{3(1+\nu)}{2E}\sigma_{ij}\sigma_{ij}\right) \quad [11]$$

Where β_j is the chemical expansion coefficient of species j; σ_{ij} is the stress tensor; $\sigma_{ij}\sigma_{ij} = \sum_{i=1}^{3}\sum_{j=1}^{3}\sigma_{ij}\sigma_{ij}$.

The chemical expansion coefficient of species j is defined as,

$$\beta_j = \frac{1}{3}\frac{\partial V_m}{V_m^0 \partial c_j} \quad [12]$$

Where V_m is the molar volume of species j in the stress-free solid with concentration of c_j; V_m^0 is the molar volume of species j in the stress-free solid with stoichiometric defect concentration of c_j^0.

The defects are considered as species that simply diffuse through a solid with a solid framework that does not change. According to non-equilibrium thermodynamics, the molar flux of the diffusing mobile defect species j is given by,

$$N_j = -\frac{c_j D_j}{RT}\nabla\mu_j \quad [13]$$

Where $D_j = RTm_j$ is the diffusion coefficient of the species j; m_j is the mobility of the species j; c_j is the concentration of diffusion component, e.g., oxygen vacancy, electron or hole.

The current density of a charged species can be represented as,

$$J_j = -\frac{z_j F c_j D_j}{RT}\nabla\mu_j \quad [14]$$

Substituting equation 10 into 14 gives,

$$J_j = -(z_j F D_j)\nabla c_j - \frac{c_j(z_j F D_j)}{RT}\nabla\tau_j - \frac{z_j F c_j (z_j F D_j)}{RT}\nabla\phi \quad [15]$$

Obviously, the current density consists of three contributors including charged species concentration gradient, stress gradient, and potential gradient.

To simplify the problem into a manageable form, we consider the case where the majority of mobile defects are vacancies and electronic species only. Because the size of electron is much smaller than that of oxygen vacancy, it is assumed that the compositional expansion is mainly caused by oxygen vacancy distribution. As a result, the effect of stress gradient on electronic current density is neglected. Also the material $Ce_{0.9}Gd_{0.1}O_{1.95-\delta}$ (GDC) is treated as a perfect electrolyte material in which the oxygen vacancy concentration is determined by the doping level only and is uniformly distributed through the entire electrolyte domain. Accordingly it is assumed that the oxygen vacancy transportation in the electrolyte is driven only by the electric field, the effects of both oxygen vacancy concentration gradient and stress gradient are neglected.

Under steady state conditions, $\nabla \cdot J_v = \nabla \cdot J_e = 0$, substituting equation 15, we have for the electrolyte and the cathode respectively,

$$\text{Electrolyte}: \nabla\cdot\left(-\frac{z_v F\overline{c_{v,0}}(z_v F D_v)}{RT}\nabla\phi\right) = 0 \quad [16]$$

Here, $\overline{c_{v,0}}$ represents the uniform oxygen vacancy concentration in the electrolyte.

Cathode :

$$\begin{cases}\nabla\cdot\left(-(z_v F D_v)\nabla c_v - \dfrac{c_v(z_v F D_v)}{RT}\nabla\tau_v - \dfrac{z_v F c_v(z_v F D_v)}{RT}\nabla\phi\right) = 0\\ \nabla\cdot\left(-(z_e F D_e)\nabla c_e - \dfrac{z_e F c_e(z_e F D_e)}{RT}\nabla\phi\right) = 0\\ \sum\limits_j z_j c_j = 0, (j = v, e, a)\end{cases} \quad [17]$$

Where v, e, and a represent vacancy, electron, and acceptor dopant respectively. The third equation in 17 characterizes the electroneutrality, requiring that the sum of all the charges in a material be equal to zero at macroscopic scale. The assumption of an electroneutrality does not necessarily preclude the existence of a nonlinear potential distribution as indicated by Newman.[22]

Model Setup and Boundary Conditions

Figure 1a shows the computational domain of the model, where a cathode particle is attached to a bulk electrolyte due to the sintering effect. It is assumed that the cathode particle is a mixed ionic and electronic conducting material, e.g., $La_{0.6}Sr_{0.4}Co_{0.2}Fe_{0.8}O_{3-\delta}$ (LSCF), while the electrolyte is an ionic conducting material, e.g., $Ce_{0.9}Gd_{0.1}O_{1.95-\delta}$ (GDC). Since the considered computational domain is relatively small, the isothermal condition is assumed. Essentially equations 9 and 16-17 need to be solved to obtain the unknowns of defect concentration c_j, potential ϕ, and solid displacements **u** as well as their derivatives. Accordingly the boundary conditions are specified including defect concentration, potential and displacement, which are detailed as follows.

Concentration boundary conditions.— The defect concentration of conducting materials is dependent on the doping level. The defect concentration also depends on the oxygen partial pressures, particularly those of bulk material surface exposed to the surrounding atmosphere, such as the cathode material $La_{0.6}Sr_{0.4}Co_{0.2}Fe_{0.8}O_{3-\delta}$ (LSCF). For perovskite-type oxides in a low oxygen partial pressure P_{O_2} and

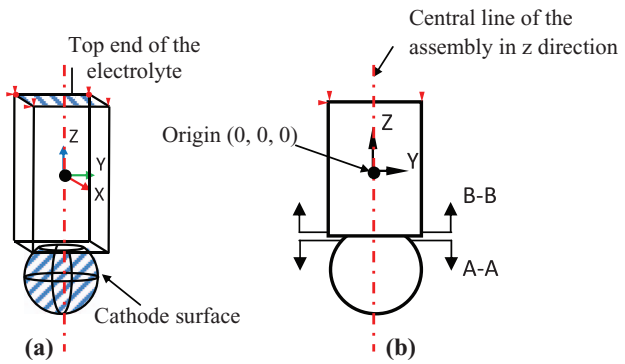

Figure 1. (a) Cathode/electrolyte assembly (the origin of XYZ coordinate system is located at the central point of the electrolyte domain); (b) schematic illustration of cross-section locations (The A-A and B-B cross sections are parallel to the cathode/electrolyte interface and have the distance of 0.5 μm from the cathode/electrolyte interface.

small temperature ranges, the oxygen nonstoichiometry δ shows linear dependence on log P_{O_2},[23,24]

$$\delta = A + B \log_{10} P_{O_2} \quad [18]$$

Where A and B are constants, depending on specific type of perovskite oxides. For $La_{0.6}Sr_{0.4}Co_{0.2}Fe_{0.8}O_{3-\delta}$ (LSCF) cathode material, A and B are obtained by fitting the experimental data,[25]

$$\delta = -0.02 - 0.03 \log_{10}(P_{O_2}/bar) \quad [19]$$

Equation 19 is valid for oxygen partial pressures from 10^{-2} bar to 10^{-8} bar and temperature at 973.15 K. It should be pointed out that for a working cathode the gas phase and the surface of the cathode particle are generally not in equilibrium,[26,27] which are assumed to be in equilibrium and the equation 19 is applicable for simplicity of the model.

Other boundary conditions.— The potential difference between the top end of the electrolyte (Figure 1a) and the cathode particle surface is determined by using the multi-physics modeling approach, which is approximately greater than or equal to −0.4 V as predicted by the SOFC model.[4] The electrolyte/cathode assembly is point-constrained at the top end of the electrolyte as shown in Figure 1a while traction-free conditions are applied on the rest of surfaces. This prevents rigid-body movements but does not affect the stress distribution. The boundary conditions are summarized in Table I.

Simulations and Model Parameters

The mathematical model is solved using finite element package, COMSOL Multiphysics V4.0. The model parameters are listed in Table II.

Since the related experimental data are very limited, the parameters noted with * are estimated based on the data from open literatures. In particular, the oxygen vacancy concentrations (c_v) induced by the dopant in the electrolyte and cathode materials are estimated according to their chemical formula. As mentioned above, the $Ce_{0.9}Gd_{0.1}O_{1.95-\delta}$ (GDC) electrolyte is treated as a perfect electrolyte, in which the oxygen vacancy concentration is uniformly distributed and determined

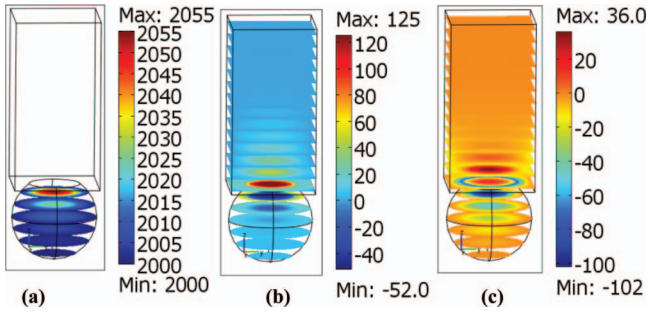

Figure 2. Oxygen vacancy concentration distribution (mol/m^3) (a); first principal stress distribution (MPa) (b); third principal stress distribution (MPa) (c).

by the dopant only. For stoichiometric defect reactions, we have δ = 0. Using the molar volume of GDC bulk electrolyte in Table II, we can obtain $\overline{c_{v,0}} = 0.05/V_{m,GDC} = 2083$ (mol/m^3). This value is used as the concentration boundary condition of the cathode/electrolyte interface. For the $La_{0.6}Sr_{0.4}Co_{0.2}Fe_{0.8}O_{3-\delta}$(LSCF) cathode particle, if choosing δ = 0.06, we can obtain $c_{v,LSCF} = 0.06/V_{m,LSCF} = 1818$ (mol/m^3). For the calculation of chemical expansion coefficient, the ratio of strain vs. oxygen nonstoichiometry is obtained from open literatures for GDC[28] and LSCF[29] respectively. The chemical expansion coefficient is then obtained by using the equation $\beta = \varepsilon/(\delta/V_m)$.

Results and Discussion

The thermal and chemical stresses are coupled together in a complicated way in practical SOFCs. It is difficult for experimental methods to identify their individual contributions. In this aspect, modeling technique has the flexibility to study the individual roles. In the following sections, the chemical stress and thermal stress are individually studied, followed by the combinational investigations.

Chemical stress.— Figure 2a shows the oxygen vacancy concentration distribution within the considered electrolyte/cathode assembly. The oxygen vacancy concentration reaches the maximum value of 2055 mol/m^3 near the cathode/electrolyte interface and decreases toward the cathode particle surface. Within the electrolyte, the oxygen vacancy concentration is uniform because the perfect electrolyte is assumed and oxygen ion transport is driven only by the electrical potential. Even though oxygen ions are generated on the cathode particle surface while being consumed at the top end of electrolyte surface in the model, the distribution of the oxygen ion concentration shows certain gradients, particularly near the cathode/electrolyte interface. This leads to the chemical stress in the cathode/electrolyte assembly.

The corresponding first principal stress and third principal stress profiles are shown in Figure 2b and Figure 2c respectively. Obviously the maximum first principal stress of 125 MPa occurs in the electrolyte near the cathode/electrolyte interface (Figure 2b). The maximum third principal stress of −102 MPa is in the cathode adjacent to the cathode/electrolyte interface (Figure 2c). Since the oxygen vacancy concentration in the cathode particle is greater than that in the cathode particle with stress-free condition (1818 mol/m^3), it tends to expand while the electrolyte is reluctant to expand. As a result, the cathode particle is in compressive state near the cathode/electrolyte

Table I. Boundary conditions.

Boundary	Oxygen vacancy concentration	Potential	Mechanics
Anode/electrolyte interface	–	0 V	Point constrained
Cathode/electrolyte interface	Specified by the doping level in electrolyte	–	Continuum
Cathode particle surface	Specified by oxygen partial pressure	$\phi_{cathode}$	Free
Other surfaces	Symmetry/Insulation, $\nabla \cdot J_v = 0$	Symmetry/Insulation $\nabla \cdot J_e = 0$	Free

Table II. Parameters used in the model.

Item Name	Cathode (LSCF)	Electrolyte (GDC)	Reference
Dimensions of computational domain (m)	Particle radius: 5×10^{-6}	$Width \times Height \times Length$ $10^{-5} \times 10^{-5} \times (2 \times 10^{-5})$	
E (GPa)	161	255.9	7
υ	0.32	0.334	7
Uniaxial tensile strength, σ_f, (MPa)	180	250	6, 31–33
ρ (kg/m^3)	6820	7150	7
T (K)	973.15	973.15	
V_m (m^3/mol)	33×10^{-6}	24×10^{-6}	28, 29
Reference oxygen vacancy concentration, (m^3/mol)	1818	–	*
Mobility $(mol \cdot m^2/J \cdot s)$	m_v: 2.0×10^{-14} m_e: 7.26×10^{-13}	m_v: 3.4×10^{-14}	34*
β (m^3/mol)	4.95×10^{-6}	–	29*
$\alpha \left(\frac{\mu m}{m} \frac{1}{K}\right)$	15	11	7

interface while the electrolyte is in tensile state. The complicated stress distribution is resulted from the combinational effects of oxygen vacancy concentration distributions and the structural configuration of the cathode/electrolyte assembly.

To examine the complicated chemical stress state across the cathode/electrolyte interface, the details of stress distributions in A-A and B-B cross sections (A-A and B-B are defined in Figure 1b) are obtained as shown in Figure 3. Figures 3a-3c and 3(c′) show the stress distributions in cross-section B-B while Figures 3d-3f and 3(f′) show those in cross-section A-A. As can be seen from Figure 3a, the shear stress distribution shows four small "islands" with relatively high stress magnitude. The positive shear stress and negative shear stress occur alternatively along the neck of the interface. According to the coordinate system defined in Figure 1a, the shear stress directions are represented with arrows in Figure 3a and 3d. The normal stress in B-B cross section shows the ring-shaped distribution (Figure 3b). Obviously the normal stress shows tensile state within a small internal circle followed by a ring band area with stress magnitude close to zero. Beyond this area, another ring band area with maximum compressive stress can be clearly seen. The normal stress then ripples off to zero toward the circumference. This phenomenon can be attributed to the non-uniform distribution of oxygen vacancy concentration in the cathode particle, where the vacancy concentration decreases from the center toward the circumference of the particle (as shown in Figure 2a). The volumetric expansions in different locations of the cathode particle will be different due to non-uniform vacancy concentrations in the cathode particle. Meanwhile the volumetric expansion of cathode particle is confined by the electrolyte at the cathode/electrolyte interface. Therefore the stress is generated as shown in Figure 3a and 3b.

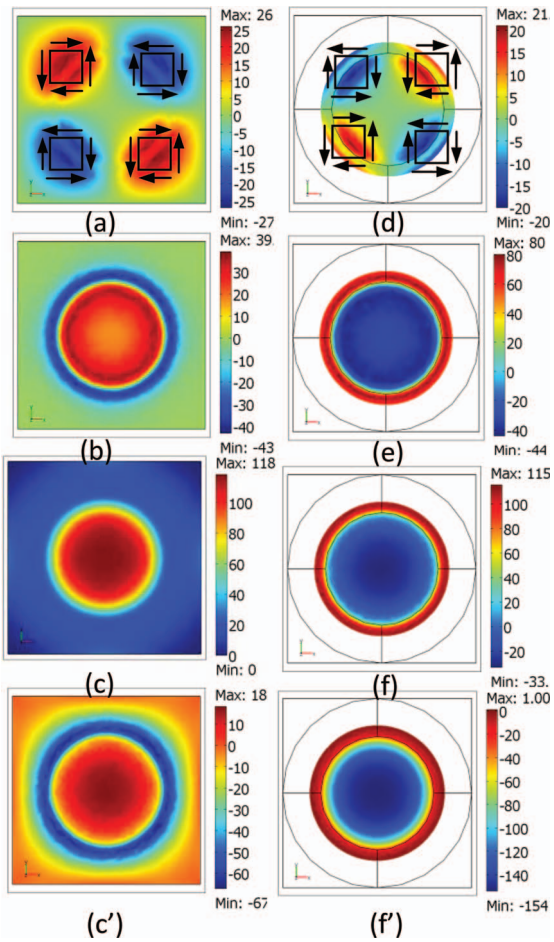

Figure 3. Chemical stress distribution (MPa). Stress at B-B cross section: (a) shear stress, (b) normal stress, (c) first principal stress, (c′) third principal stress; stress at A-A cross section: (d) shear stress, (e) normal stress, (f) first principal stress; (f′) third principal stress.

The first and third principal stresses in the B-B cross-section in the electrolyte are shown in Figures 3c and 3(c′) respectively. The first principal stress in Figure 3c shows the maximum value of 118 MPa in the central circle area and ripples to zero toward the circumference. Obviously the maximum first principal stress of 118 MPa is less than the uniaxial tensile strength 250 MPa of the GDC electrolyte (Table II). The third principal stress in Figure 3(c′) shows tensile state within the central circle area followed by the maximum compressive stress of −67 MPa in a ring band. The third principal stress then decreases to a relative low compressive stress state toward the circumference. For ceramic materials, the compressive strength is usually greater than the tensile strength. Due to the lack of experimental data, here we assume that the compressive strength is equal to the tensile strength for the GDC electrolyte. Accordingly the maximum third principal stress of −67 MPa is less than the compressive strength of −250 MPa. Comparing the first and third principal stresses in B-B cross-section with the GDC electrolyte strength, one can see that the chemical stress will not lead to the fracture of the electrolyte.

The various stress distributions in A-A cross section in the cathode particle are shown in Figure 3d-3f and 3(f′), which display opposite distribution patterns to those in B-B cross section. These results can be attributed to the balance requirement of stresses in the cathode/electrolyte assembly. The maximum first principal stress takes place in the shell area of the cathode particle and reaches 115 MPa as shown in Figure 3f. The maximum third principal stress occurs in the central circle area and reaches −154 MPa as shown in Figure 3(f′). Obviously it is in compressive stress state. Here we assume that the compressive strength of LSCF material is the same as its tensile strength (180 MPa) due to the lack of experimental data. One

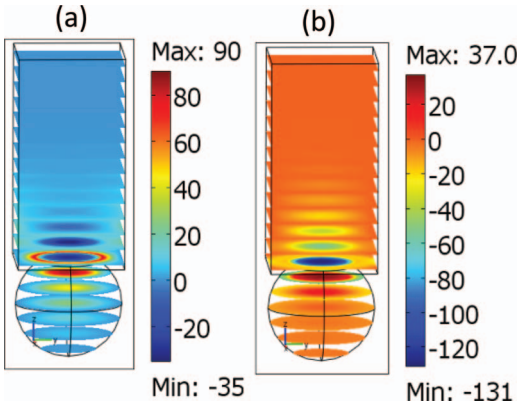

Figure 4. Distribution of principal stresses (MPa): (a) first principal stress; (b) third principal stress.

can see that neither the first principal stress nor the third principal stress can lead to the fracture of the cathode particle.

Thermal stress.— Since the computational domain is relatively small, the temperature distribution is assumed to be uniform within the domain. Accordingly the thermal stress is calculated by varying the temperature from one state to another. Because the LSCF cathode is generally sintered at 900–1000°C,[30] the stress-free temperature is assumed at 1000°C. The thermal stress is then calculated when the cathode/electrolyte assembly is operated at 700°C. Figures 4a and 4b show the corresponding first and third principal stress distributions respectively. Clearly the maximum stress occurs at the cathode/electrolyte interface with significant non-uniformity. Since the assumed operating temperature (700°C) is different from the thermal stress-free temperature (1000°C), and thermal expansion coefficient of GDC electrolyte is different from that of LSCF cathode, the expansion of the GDC electrolyte should be different from that of the LSCF cathode. However, without delamination, the expansion of both electrolyte and cathode should be identical at the cathode/electrolyte interface. This confliction of structural deformation leads to the thermal stress as shown in Figure 4.

To examine the details of thermal stress near the cathode/electrolyte interface and identify the difference from their chemical stress counterparts, the distribution of stress components is individually obtained at the cross sections A-A and B-B respectively. The shear stress distribution in B-B cross section shows four small "islands" (Figure 5a), where the positive and negative shear stress "islands" appear alternatively. Comparing the chemical stress distribution in the same cross section B-B (Figure 3a), one can see that the pattern of thermal stress distribution in Figure 5a is opposite to that of chemical stress distribution. The difference of stress distribution is due to the different natures of chemical expansion and thermal expansion, where the chemical expansion is the tendency of materials to change in volume due to the variations of oxygen vacancy concentration; whereas the thermal expansion is the tendency of materials to change their volumes in response to the change in temperatures. The normal stress in B-B cross section shows a ring-band distribution (Figure 5b). Within a central circle, the normal stress is compressive. Beyond this central circle area, a ring band with normal stress amplitude close to zero can be observed, followed by another ring-band like area, in which the normal stress is tensile. The stress then decays to zero toward the circumference.

The first and third principal stress distribution in B-B cross section is shown in Figure 5c and 5(c′) respectively. The first principal stress in Figure 5c is in compressive state in the central circle area. Beyond this circle area, a ring-band area appears with the maximum tensile stress of 76 MPa. The first principal stress then decays to 0 MPa toward the circumference. The third principal stress in Figure 5(c′) shows the maximum compressive stress of −124 MPa within the central circle

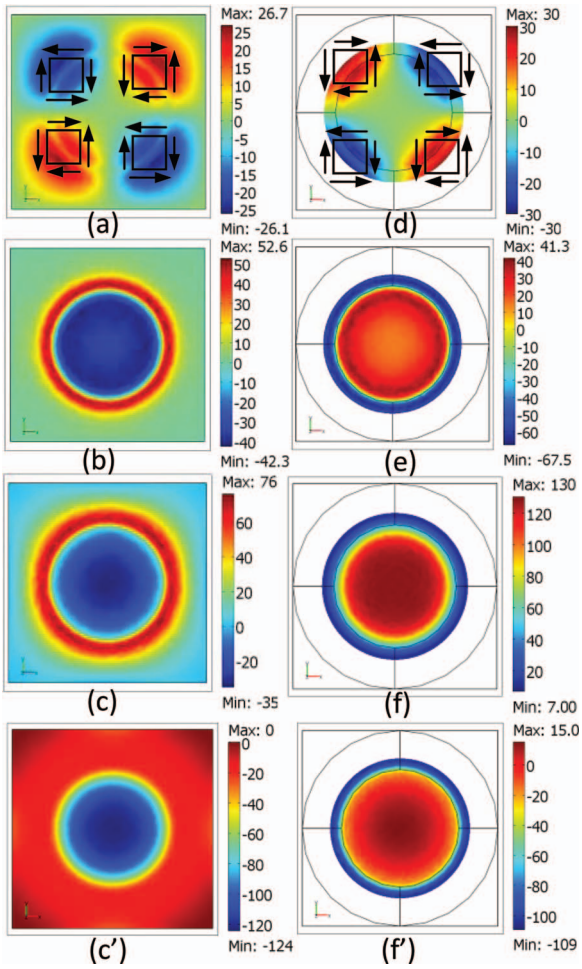

Figure 5. Thermal stress distribution (MPa). Stress at B-B cross section: (a) shear stress, (b) normal stress, (c) first principal stress, (c′) third principal stress; stress at A-A cross section: (d) shear stress, (e) normal stress, (f) first principal stress; (f′) third principal stress.

area. Beyond this circle, the third principal stress decays to 0 MPa. Since both the maximum first principal stress and the maximum third principal stress are less than the strength of the GDC electrolyte, the thermal stress cannot cause the failure of the GDC electrolyte.

The various thermal stress distributions in A-A cross section in the cathode particle are shown in Figure 5d-5f and 5(f′), which display opposite distribution patterns to those in B-B cross section. These results may be attributed to the balance requirement of stresses in the cathode/electrolyte assembly due to the mismatch of thermal expansion coefficients between the electrolyte and the cathode. The maximum first principal stress takes place within the central circle area and reaches 130 MPa as shown in Figure 5f. The maximum third principal stress occurs in the shell area of the cathode particle circumference and reaches −109 MPa as shown in Figure 5(f′). Obviously it is in compressive stress state. Since the tensile/compressive strength of the LSCF cathode is 180 MPa (Table II), we can see that neither the first principal stress nor the third principal stress can lead to the fracture of the cathode particle.

Combined chemical and thermal stresses at the cathode/electrolyte interface.— In practical solid oxide fuel cells, the chemical stress and thermal stress occur simultaneously. In this section, the cathode/electrolyte interfacial stresses induced by the combined chemical and thermal effects are studied. The operating conditions are the combination of those in previous sections of chemical stress and thermal stress. Comparing every single chemical stress distribution in

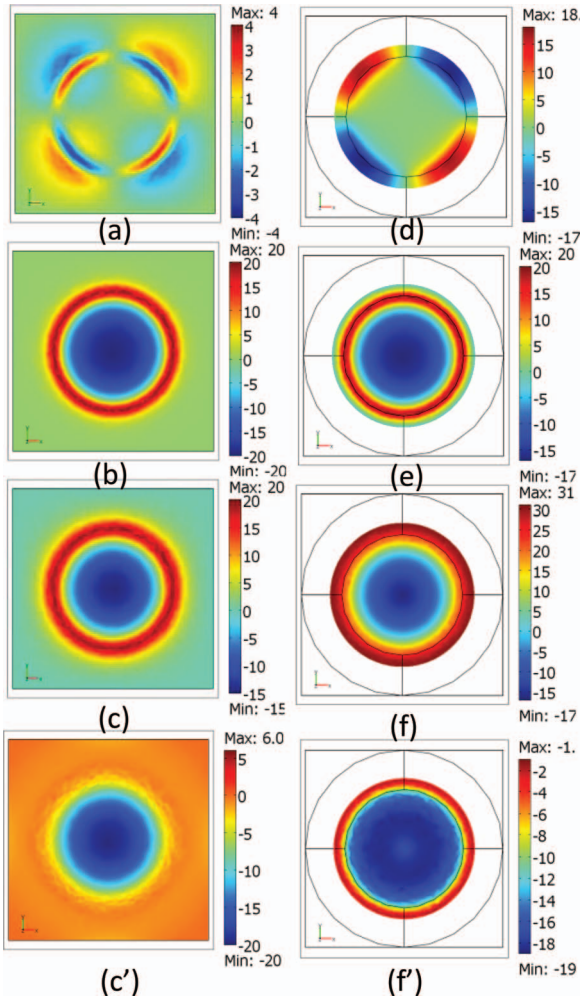

Figure 6. Combined thermal and chemical stress (MPa). In B-B cross section: (a) shear stress, (b) normal stress, (c) first principal stress, (c′) third principal stress; In A-A cross section: (d) shear stress, (e) normal stress, (f) first principal stress; (f′) third principal stress.

Figure 3 with the corresponding thermal stress distribution in Figure 5, one may find that the patterns of chemical stress distribution are opposite to those of thermal stress distribution. Therefore the chemical stress will be partially canceled out by the thermal stress, or vise verse, when combined together. This understanding can be seen from Figure 6, where the magnitude of every single combinational stress is less than that of chemical stress (Figure 3) and thermal stress (Figure 5). So the combination of chemical and thermal stress facilitates to mitigate the overall stress occurred at the cathode/electrolyte interface. In B-B cross section, the maximum first principal stress is the tensile stress of 20 MPa (Figure 6c) and the maximum third principal stress is the compressive stress of −20 MPa (Figure 6(c′)), both of which are less than the strength of the GDC electrolyte (Table II). Therefore no fracture occurs in the electrolyte in this case. Similarly, in A-A cross section, the maximum first principal stress is the tensile stress of 31 MPa (Figure 6f) and the maximum third principal stress is the compressive stress of −19 MPa (Figure 6(f′)), both of which are less than the strength of the LSCF cathode (Table II). Therefore no fracture occurs in the cathode particle either.

Effects of non-uniform oxygen partial pressure.— Oxygen partial pressure may significantly affect the surface oxygen vacancy concentration of cathode material and oxygen reduction reaction process. At the cathode side of SOFCs, the oxygen diffuses from the channel to

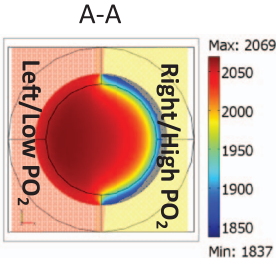

Figure 7. Oxygen vacancy concentration distribution at A-A cross section.

the surface of cathode material through porous electrode. As a result, non-uniform oxygen partial pressure distribution may exist within porous cathode. It is anticipated that the non-uniform distribution of oxygen partial pressure could cause complicated chemical stress and ceramic particle distortions. To study such effects, we assume that different portion of cathode particle surface (shown in Figure 7) is subjected to different oxygen partial pressures. Specifically, the oxygen partial pressure of 0.002 bar is applied to the right half surface of the cathode particle, while that of 0.00112 bar is applied to the left half surface of the cathode particle (Figure 7). The rest of the operating conditions are the same as those in chemical stress section. Because of non-uniform oxygen partial pressure on the cathode particle, the corresponding distribution of oxygen vacancy concentration within the A-A cross section is also non-uniform (Figure 7). Specifically, the right half surface of the cathode particle is exposed to the environment with high oxygen partial pressure; consequently the concentration of oxygen vacancy is low. This can be seen from the shell area of the right half surface of the cathode particle in Figure 7. By contrast, the left half surface of the cathode particle is exposed to the low oxygen partial pressure; as a result, the corresponding concentration of oxygen vacancy is high, because the gas phase and the surface of the cathode particle are in equilibrium. One may also see from Figure 7 that the oxygen vacancy concentration within the central circle area is high, which is significantly affected by low oxygen partial pressure instead of high oxygen partial pressure.

The higher oxygen vacancy concentration leads to larger expansions in volume, therefore, the non-uniform distribution of oxygen vacancy concentration is expected to cause the complicated chemical stress distribution. Figure 8a shows the first principal stress in A-A

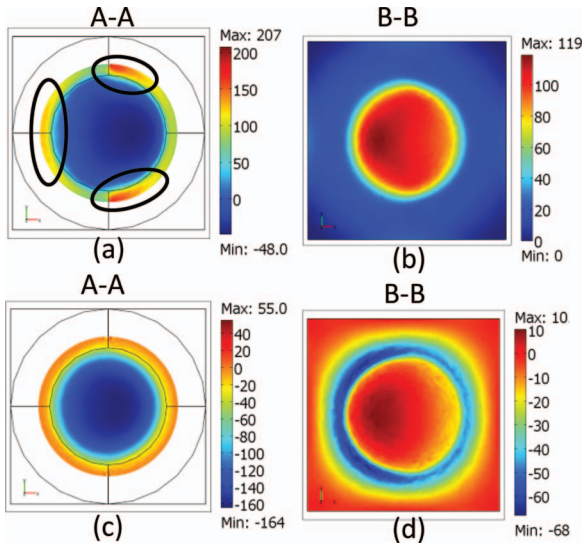

Figure 8. principal stress distributions (MPa) under non-uniform oxygen partial pressure. (a) first principal stress at A-A cross section, (b) first principal stress at B-B cross section; (c) third principal stress at A-A cross section, (d)) third principal stress at B-B cross section.

cross section, which shows significant variations along the circumferential shell area of the cathode particle. The first principal stress in Figure 8a varies from −48 MPa to 207 MPa, which exceeds the fracture strength of the LSCF cathode material 180 MPa. As a result, cracks within the cathode particle might initiate in this case. It is worth noting that the assumption of abrupt changes of oxygen partial pressure on the cathode particle surface might be an extreme scenario, however, the results clearly demonstrate the significant effects of oxygen partial pressure on chemical stress generation. The third principal stress in Figure 8c is dominated by the compressive stress within the central area of A-A cross section.

As shown in Figure 7, the distribution of the oxygen vacancy concentration is significantly non-uniform. It has been realized that different vacancy concentrations lead to different volumetric expansions in the material. On the other hands, such volumetric expansions are also confined by the structure configuration of the cathode/electrolyte assembly. Therefore complicated stress takes place. The first and third principal stresses in B-B cross section are shown in Figure 8b and 8d respectively. The maximum tensile stress is 119 MPa while the maximum compressive stress is −68 MPa. None of these stresses can lead to the cracks within the GDC electrolyte (strength 250 MPa). Comparing to Figures 3c, 3(c′), 3f and 3(f′), one can see that the stress distributions in Figure 8a-8d show different degree of distortion because of non-uniform oxygen partial pressure distribution on the cathode particle surface.

Effects of oxygen vacancy concentration at the cathode particle surface.— For practical solid oxide fuel cells, the cathode is exposed to the environment containing oxygen gas. The oxygen gas in turn affects the surface oxygen vacancy concentration of the cathode particle, which will further influence the oxygen vacancy concentration distribution in the cathode/electrolyte assembly. Figure 9a shows the distribution of oxygen vacancy concentration. The horizontal axis in Figure 9 is defined from the cathode surface toward the cathode/electrolyte interface along the central line of the cathode/electrolyte assembly in z-direction (the z-direction is defined in Figure 1a). The dimension from −19 μm to −10 μm on the horizontal axis is the cathode domain while that from −10 μm to 10 μm is the electrolyte domain. As shown in Figure 9a, the oxygen vacancy concentration increases from the cathode particle surface to the cathode/electrolyte interface. The gradient of the oxygen vacancy concentration is relatively large near the cathode/electrolyte interface. When the oxygen vacancy concentration increases from 1800 mol/m^3 to 2000 mol/m^{3}at the cathode surface, the overall distribution of oxygen vacancy concentration also increases. The corresponding distributions of the normal stress, the first principal stress, and the third principal stress are shown in Figure 9b, 9c, and 9d respectively. Obviously the maximum stress and the maximum stress gradient take place near the cathode/electrolyte interface, where the compressive stress occurs at the cathode side while the tensile stress happens at the electrolyte side. Since the oxygen vacancy

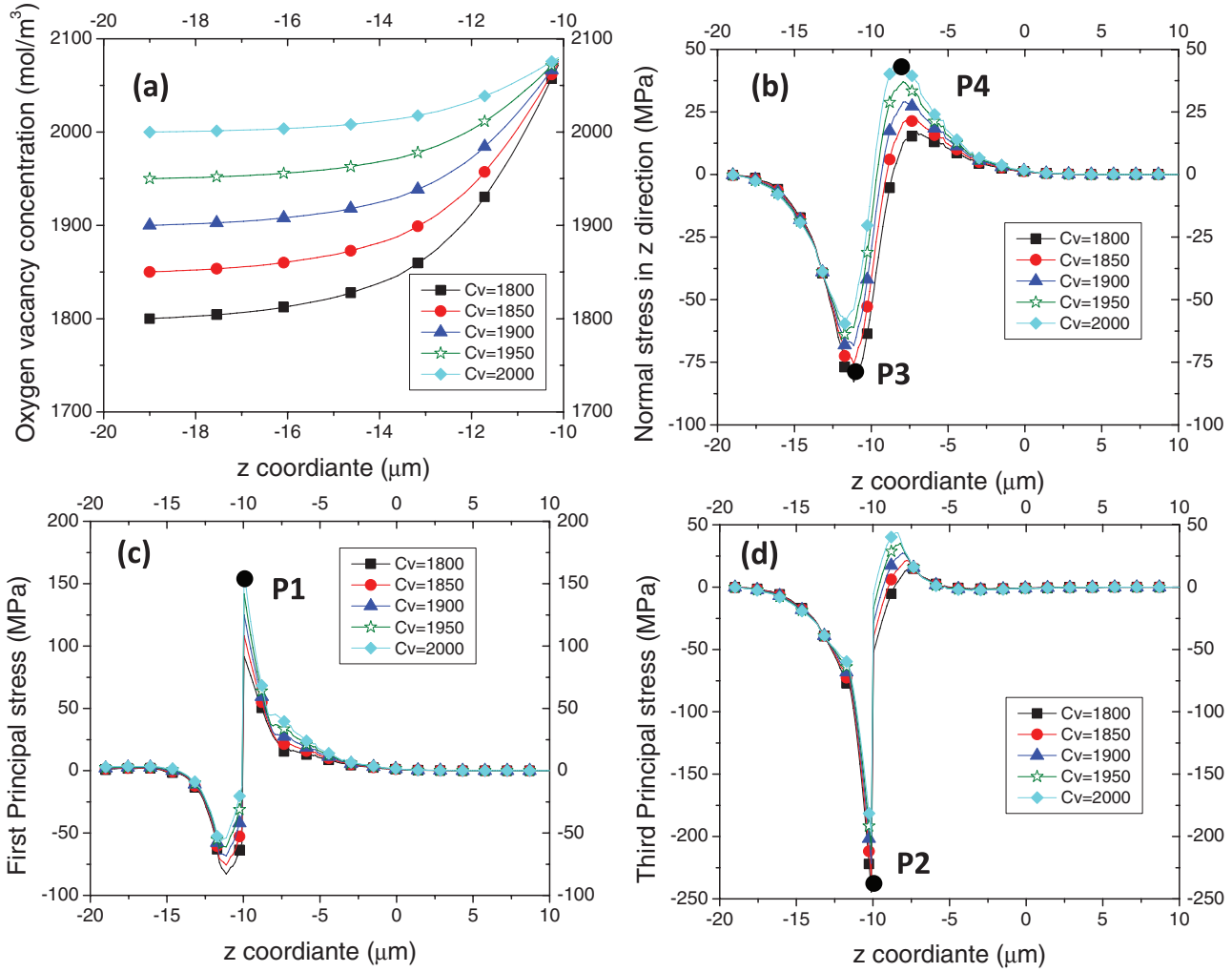

Figure 9. Parameter distribution along the central line of the cathode/electrolyte assembly in z-direction under different oxygen partial pressure: (a) oxygen vacancy concentration, (mol/m^3); (b) normal stress in z direction, (MPa); (c) first principal stress, (MPa). (d) third principal stress, (MPa).

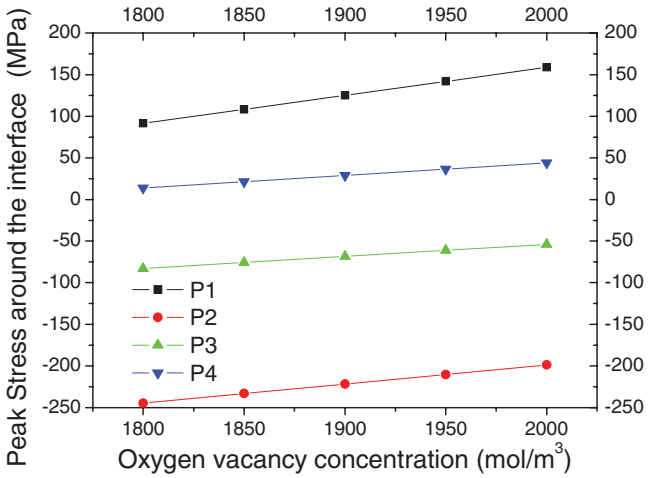

Figure 10. Peak stress at the specified locations in Figure 9, (MPa).

concentration reaches the maximum value at the cathode/electrolyte interface and decreases toward the cathode particle surface (as shown in Figure 9a), the volumetric expansion of cathode near the cathode/electrolyte interface is larger than that of the rest part in the cathode. Considering that the cathode expansion near the cathode/electrolyte interface is confined by the electrolyte, this is the reason that the compressive stress occurs at the cathode side while the tensile stress takes place at the electrolyte side. To correlate the boundary conditions on the cathode surface with the maximum stresses occurred at the cathode/electrolyte interface, four peak stresses marked as P1, P2, P3, and P4 in Figure 9c, 9d, and 9b respectively are selected. Figure 10 shows the correlations between P1, P2, P3, P4 and the oxygen vacancy concentrations on the cathode particle surface. P1 and P4 are in tensile state while P2 and P3 are in compressive state. Clearly, increasing the oxygen vacancy concentration on the cathode particle surface will increase the tensile stresses of P1 and P4 but decrease the compressive stresses of P2 and P3. Conversely, decreasing the oxygen vacancy concentration on the cathode particle surface is beneficial to reduce the tensile stresses of P1 and P4 but increase the compressive stresses of P2 and P3. Therefore, suitable oxygen vacancy concentration on the cathode particle surface needs to be considered so that the first and third principal stresses can be confined below the strength of the concerned materials if appropriate.

Conclusions

A micro model is developed to study the cathode/electrolyte interfacial stresses. The model considers the complicated interactions between structural mechanics and ionic transport process through conductive defects. While both the chemical and thermal stresses are complicated at the interface, the chemical stresses show different distribution patterns from the thermal stresses. The results of combined thermal and chemical stresses show that these two kinds of stresses can be partially canceled out with each other, leading to the reduced overall stresses at the cathode/electrolyte interface. The distributions of oxygen partial pressure and thus the oxygen vacancy concentration on the cathode particle surface have significant effects on chemical stress distribution and consequently on the principal stresses at the cathode/electrolyte interface.

Acknowledgment

The authors gratefully acknowledge the National Science Foundation for financial support under grant no. CMMI-1100085.

List of Symbols

c_j, (mol/m^3)	Concentration of species/defects j
$\overline{c_{v,0}}$, (mol/m^3)	the uniform oxygen vacancy concentration in electrolyte
D_j, (m^2/s)	Diffusion coefficient of defects j
E, (GPa)	Young's Modulus
F, (C/mol)	Faraday's constant, 96485
J_j, (A/m^2)	Current density of species j
K, $atm^{1/2}$	Equilibrium constant
m_j, $(m^2 \cdot mol/(J \cdot s))$	Mobility of species j
N_j, $(mol/(m^2 \bullet s))$	Flux of species j
P, (Pa)	Pressure
R, $(J/(mol \bullet K))$	Gas constant, 8.314
T, (K)	Temperature
u, (m)	Displacement (**Vector**)
V_m, (m$^3/mol$)	Molar volume of the material
x_j	Molar fraction of species j
z_j	Effective charge of species j

Greek symbols

ρ, (kg/m^3)	Density
α, $(\frac{\mu m}{m}\frac{1}{K})$	Thermal expansion coefficient
β, (m^3/mol)	Chemical expansion coefficient
ν	Poisson's ratio
ε_{ij}	Strain tensor
σ_{ij}, (N/m^2)	Stress tensor
σ_{kk}, (N/m^2)	$\sigma_{kk} = \sigma_1 + \sigma_2 + \sigma_3$
τ_j, (J/mol)	Stress induced potential by species j
μ_j, (J/mol)	Electrochemical potential of species j
ϕ, (V)	Potential
δ	Oxygen nonstoichiometry

Subscripts

a	Dopant
f	fracture
e	Electron
j	Species j
v	Oxygen vacancy

Superscripts

me	Mechanical
T	Thermal
c	Chemical
0	Stoichiometric

References

1. A. Weber, *Fuel Cells-Solid Oxide Fuel Cells / Life-Limiting Considerations*, in *Encyclopedia of Electrochemical Power Sources*. 2009. p. 120–134.
2. K. Park et al., *International Journal of Hydrogen Energy*, **35**(16), 8670 (2010).
3. A. V. Virkar, *International Journal of Hydrogen Energy*, **35**(18), 9527 (2010).
4. X. F. Jin and X. J. Xue, *International Journal of Hydrogen Energy*, **35**(14), 7321 (2010).
5. R. S. Gemmen and C. D. Johnson, *Journal of Power Sources*, **159**(1), 646 (2006).
6. G. Anandakumar et al., *Journal of Power Sources*, **195**(19), 6659 (2010).
7. M. F. Serincan, U. Pasaogullari, and N. M. Sammes, *Journal of Power Sources*, **195**(15), 4905 (2010).
8. K. Huang and H. D. Harter, *Solid State Ionics*, **181**(19-20), 943 (2010).
9. T. L. Jiang and M. H. Chen, *International Journal of Hydrogen Energy*, **34**(19), 8223 (2009).
10. L. Liu, G. Y. Kim, and A. Chandra, *Journal of Power Sources*, **195**(8), 2310 (2010).
11. A. Selimovic et al., *Journal of Power Sources*, **145**(2), 463 (2005).
12. M. Ettler et al., *Journal of Power Sources*, **195**(17), 5452 (2010).

13. S. R. Bishop, K. L. Duncan, and E. D. Wachsman, *Electrochimica Acta*, **54**(5), 1436 (2009).
14. K. Sato et al., *Journal of Power Sources*, **195**(17), 5481 (2010).
15. K. L. Duncan et al., *Journal of the American Ceramic Society*, **89**(10), 3162 (2006).
16. S. B. Adler, *Journal of the American Ceramic Society*, **84**(9), 2117 (2001).
17. N. Swaminathan and J. Qu, *Fuel Cells*, **7**(6), 453 (2007).
18. S. P. Timoshenko and J. N. Goodier, *Theory of Elasticity*. 1970, New York: McGraw-Hill.
19. N. Noda, R. B. Hetnarski, and Y. Tanigawa, *Thermal Stresses*. 2nd ed. 2003, New York: Taylor & Francis.
20. N. Swaminathan, J. Qu, and Y. Sun, *Philosophical Magazine*, **87**(11), 1705 (2007).
21. N. Swaminathan, J. Qu, and Y. Sun, *Philosophical Magazine*, **87**(11), 1723 (2007).
22. J. Newman, *Electrochemical Systems*. 1991, NJ: Prentice-Hall, Englewood Cliffs.
23. J. Mizusaki et al., *Journal of Solid State Chemistry*, **58**(2), 257 (1985).
24. Y. Zeng and Y. S. Lin, *Solid State Ionics*, **110**(3-4), 209 (1998).
25. S. Hashimoto et al., *Solid State Ionics*, **181**(37-38), 1713 (2010).
26. S. B. Adler, J. A. Lane, and B. C. H. Steele, *Journal of the Electrochemical Society*, **143**(11), 3554 (1996).
27. J. Fleig and J. Maier, *Journal of the European Ceramic Society*, **24**(6), 1343 (2004).
28. A. Atkinson, *Solid State Ionics*, **95**(3-4), 249 (1997).
29. A. Atkinson and T. M. G. M. Ramos, *Solid State Ionics*, **129**(1-4), 259 (2000).
30. D. Gostovic et al., *Electrochemical and Solid State Letters*, **10**(12), B214 (2007).
31. A. Nakajo et al., *Ceramics International*, **38**(5), 3907 (2012).
32. A. Atkinson and A. Selcuk, *Solid State Ionics*, **134**(1-2), 59 (2000).
33. Y. H. Du et al., *Journal of the Electrochemical Society*, **150**(1), A74 (2003).
34. K. L. Duncan and E. D. Wachsman, *Journal of the Electrochemical Society*, **156**(9), B1030 (2009).